

Young Galaxy Candidates in the Hubble Frontier Fields.

I. Abell 2744

Wei Zheng¹, Xinwen Shu^{2,3}, John Moustakas⁴, Adi Zitrin^{5,6}, Holland C. Ford¹, Xingxing Huang^{1,3}, Tom Broadhurst^{7,8}, Alberto Molino⁹, Jose M. Diego¹⁰, Leopoldo Infante¹¹, Franz E. Bauer^{11,12}, and Daniel D. Kelson¹³

ABSTRACT

We report the discovery of 18 Lyman-break candidates at $z \gtrsim 7.0$, in the completed WFC3/IR data Hubble Frontier Fields (HFF) observations of Abell 2744 ($z = 0.308$), plus *Spitzer*/IRAC data and archival ACS data. Half of these candidates fall in the range $8 < z < 9$, but no convincing detection lies beyond, despite the extreme depth and lens magnification. The sample includes a triple image system with a photometric redshift of $z \simeq 7.4$. This high redshift is geometrically confirmed by our lens model corresponding to deflection angles that are 12% larger than the lower-redshift systems used to calibrate the lens model at $z = 2.019$. The majority of our high-redshift candidates are not expected to be multiply lensed given their locations in the image plane, but are magnified by factors of $1.3 - 5.9$, so that we are seeing further down the luminosity function than comparable deep field imaging. It is apparent that the redshift distribution of these sources does not smoothly extend over the full redshift range accessible at $z < 12$, but appears to break above $z = 8.5$. Nine candidates are clustered within a small region of $20''$ across, and so it will be necessary to average over the additional HFF clusters to properly examine this potentially steep transition in galaxy density at $z \simeq 8 - 9$. The physical properties of our candidates are examined using the range of lens models developed for the HFF program by various groups including our own, for a better estimate of underlying systematics. Our spectral-energy-distribution fits for the brightest objects suggest stellar masses of $\simeq 10^9 M_\odot$, star-formation rates of $\simeq 5 M_\odot \text{ yr}^{-1}$, and a typical formation redshift of $z \lesssim 16$. The upcoming deep optical data will be helpful in extending the utility of the very deep near-infrared data and potentially enhancing the numbers of lower-luminosity dropout galaxies at $z > 7$.

Subject headings: cosmology: observation - galaxies: clusters: individual: Abell 2744 - galaxies: high-redshift - gravitational lensing: strong

¹Department of Physics and Astronomy, Johns Hopkins University, Baltimore, MD 21218

²CEA Saclay, DSM/Irfu/Service d'Astrophysique, Orme des Merisiers, 91191 Gif-sur-Yvette Cedex, France

³Department of Astronomy, University of Science and Technology of China, Hefei, Anhui 230026, China

⁴Department of Physics and Astronomy, Siena College, Loudonville, NY 12211

⁵Cahill Center for Astronomy and Astrophysics, California Institute of Technology, MS 249-17, Pasadena, CA 91125

⁶Hubble Fellow

⁷Department of Theoretical Physics, University of Basque Country UPV/EHU, Bilbao, Spain

⁸IKERBASQUE, Basque Foundation for Science, Bil-

bao, Spain

⁹Instituto de Astrofísica de Andalucía - CSIC, Glorieta de la Astronomía, s/n. E-18008, Granada, Spain

¹⁰IFCA, Instituto de Física de Cantabria, UC-CSIC, s/n. E-39005 Santander, Spain

¹¹Pontificia Universidad Católica de Chile, Instituto de Astrofísica, Santiago 22, Chile

¹²Space Science Institute, Boulder, CO 80301

¹³The Observatories of the Carnegie Institution for Science, Pasadena, CA 91101

1. INTRODUCTION

Our understanding of the first few billion years of cosmic time has increased significantly in recent years, thanks to the *Hubble Space Telescope's* (HST) Wide-Field Camera 3/Infrared Channel (WFC3/IR, Kimble et al. 2008) as well as the *Spitzer Space Telescope's* Infrared Array Camera (IRAC, Fazio et al. 2004). Until recently, the Hubble Ultra Deep Field (Beckwith et al. 2006; Illingworth et al. 2013) has provided our deepest view of the Universe, revealing a considerable number of galaxy candidates at $z > 7$, including one candidate at $z \simeq 10$ (Bouwens et al. 2011, 2012a; Ellis et al. 2013; Oesch et al. 2013; Illingworth et al. 2013). The cosmic epoch of $z \simeq 10$ is important to study as it marks the dawn of galaxy formation and the beginning of reionization of the intergalactic medium. However, galaxies at that redshift are extremely faint, making it difficult to discover and study the abundant population of galaxies below L^* , the knee of the luminosity function. Fortunately, the magnification boost afforded by gravitational lensing combined with HST's exquisite imaging capabilities in the near-infrared (NIR), provides an avenue for both discovering and characterizing the intrinsic properties of galaxies around $z \simeq 12$, when the Universe was less than half a billion years old.

The Cluster Lensing And Supernova survey with Hubble (CLASH, Postman et al. 2012) carried out HST imaging of 25 galaxy clusters in 16 broad bands between $0.2\text{--}1.7\ \mu\text{m}$ to a depth of AB magnitude ~ 27 with a total of 20 orbits per cluster. The CLASH program has led to many interesting discoveries of magnified, intrinsically faint galaxies. Several hundred dropout galaxies have been uncovered in the range $z \simeq 6\text{--}8$, with a few notable examples at higher redshifts of $z \simeq 9\text{--}11$ (see Zheng et al. 2012; Bouwens et al. 2012b; Coe et al. 2013; Bradley et al. 2013), helping to motivate dedicated deeper lensing surveys.

The Hubble Frontier Fields (HFF) is a new initiative now being carried out to observe the distant Universe to an unprecedented depth, combining the power of deep HST imaging and gravitational lensing. In HST's Cycles 21 and 22, 560 orbits of Director's Discretionary Time have been allocated to observe four clusters. The observations are carried out with four WFC3/IR filters (F160W,

F140W, F125W, F105W) and three ACS filters (Advanced Camera for Surveys, Ford et al. 1998, F814W, F606W, F435W). It is anticipated that 280 orbits will be allocated in Cycle 23 to observe two additional clusters. In addition, deep *Spitzer* and *Chandra* observations are planned for the six HFF fields. These coordinated observations will enable us to probe the star formation rate density at $z \gtrsim 9$, study the faint end of the galaxy population at $z \simeq 3\text{--}8$, and map the dark matter in these clusters in unprecedented detail via many multiple images of background sources (Hubble Deep Fields Initiative 2012 Science Working Group Report).¹⁴

We report the discovery of 18 candidates of Lyman-break galaxies (LBGs) at $z \gtrsim 7$ in the field of Abell 2744, based on the first epoch of HFF NIR observations and archival optical ACS data. The faintest sources detected are around AB magnitude 28.5. We rank our candidates into two groups: The first group consists of 14 objects with “secure” photometric redshifts greater than 7 and a negligible probability ($< 1\%$) of being at lower redshift. Four other objects (Group 2) have photometric redshifts greater than 7, but with a non-negligible probability of being at lower redshift. These objects, listed in Tables 2 and 3, are selected with confidence, and future deep ACS observations will likely only further diminish the probability that they are lower-redshift interlopers. In addition to these 18 candidates, four other objects (Table 4) have NIR colors that meet our selection criteria, but their estimated photometric redshifts suggest lower-redshift solutions ($z < 3$). For these potential candidates the photometric redshift probability distribution is bimodal; therefore, we consider both high- and low-redshift solutions to be possible until deeper optical imaging, particularly in the F814W band, becomes available.

We adopt a concordance cosmology with $\Omega_M = 0.3$, $\Omega_\Lambda = 0.7$ and $h = H_0/100\text{ km s}^{-1}\text{ Mpc}^{-1} = 0.7$, and the AB magnitude system throughout.

2. DATA

Abell 2744 ($z = 0.308$) is the first HFF target in HST's Cycle 21. It is one of the most actively merging galaxy clusters known (Merten et al.

¹⁴<http://www.stsci.edu/hst/campaigns/frontier-fields/HDFLSWGReport2012.pdf>

2011), displaying a large critical curve of roughly $60'' \times 30''$. The six HFF clusters have been selected to maximize the lensing boost, which means that systems with highly complex mass distributions (*e.g.*, clusters in the process of merging) have been selected (Torri et al. 2004; Redlich et al. 2012; Zitrin et al. 2013b). The WFC3/IR observations of Abell 2744 (GO/DD 13495, PI: Lotz) were carried out between 2013 Oct. 25 and Nov. 28. Additional data of one orbit in the F160W and F105W bands were taken in 2013 Aug. (GO 13386, PI: Rodney). The ACS images were obtained in 2009 (GO 11689, PI: Dupke) and retrieved from the Mikulski Archive for Space Telescopes (MAST¹⁵). Table 1 lists the exposure times and limiting AB magnitudes for all the imaging used in our analysis. Deep ACS observations are planned for the summer of 2014 (70 orbits), which will increase the depth of the optical imaging by ~ 0.9 magnitude.

We process the *HST* data using APLUS (Zheng et al. 2012), an automated pipeline modified from the APSIS package (Blakeslee et al. 2003) with an enhanced capability of processing WFC3 data and aligning them with the ACS data. We retrieve the calibrated images from the *HST* instrument pipelines, namely the *flc* images for ACS (corrected for the detector charge transfer efficiency) and *flt* images for WFC3/IR. Recently, we have updated APLUS so that images of individual exposures are aligned using *DrizzlePac* (Hack, Dencheva & Fruchter 2013), achieving an astrometric precision of $\sim 0''.015$ or better.

Using APLUS, we align, resample, and combine all the available imaging in each filter to a common pixel scale of $0''.065$, which is a half WFC3/IR's pixel scale and slightly larger than that of ACS. We then create detection images from the inverse-variance weighted sum of the WFC3/IR and ACS images, respectively, and run SExtractor (Bertin & Arnouts 1996) in dual-image mode. We choose colors measured from isophotal magnitudes to select our high-redshift candidates (see §3), as they balance the need between depth and photometric precision (Ferguson & McGaugh 1995). The 5σ limiting magnitude in the WFC3/IR bands is ~ 28.9 in a $0''.4$ diameter aperture (see Table 1); for the observed-frame optical ACS bands the 1σ limiting magnitude is ~ 30 .

As part of the HFF campaign, deep *Spitzer*/IRAC images were obtained in 2013 Sep. in Channels 1 and 2 at wavelengths $3.1 - 3.9$ and $3.9 - 5.0$ μm , respectively, using Director's Discretionary Time (Program 90257, PI: Soifer). The total exposure time, including the archival data (Program 84; PI: Rieke) obtained in 2004, is ~ 350 ksec. The IRAC corrected Basic Calibrated Data (cBCD) images are processed with MOPEX (Makovoz & Khan 2005) and sampled to a final pixel scale of $0''.6$. The estimated 1σ limiting magnitude is 27.3 for IRAC channel 1 (IRAC1, $3.6\mu\text{m}$) and 27.1 for channel 2 (IRAC2, $4.5\mu\text{m}$; see Table 1).

3. SELECTION

We search for LBGs using their distinct color around $0.1216(1+z)$ μm . For example, at $z \simeq 7-8$, the Lyman break is at ~ 1 μm , between the F814W and F125W bands. Our selection criteria, in units of magnitude, are as follows:

$$F814W - F105W > 0.8$$

$$F105W - F125W < 0.6$$

$$F814W - F105W > 0.8 + (F105W - F125W)$$

These color cuts are similar to those utilized in previous work such as Oesch et al. (2010).

For $z \simeq 8-9$, the break is at ~ 1.15 μm , between the F105W and F140W bands:

$$F105W - F140W > 0.8$$

$$F140W - F160W < 0.6$$

$$F105W - F140W > 0.8 + (F140W - F160W)$$

And for $z \simeq 10$, the break is between the F125W and F160W bands:

$$F125W - F160W > 0.8$$

The archival ACS images of Abell 2744 have a total exposure time four times longer than that of a typical CLASH cluster in each band, making it possible to constrain the photometric redshifts of candidates at magnitudes $\lesssim 28.5$, *i.e.*, one magnitude deeper than the nominal limit of CLASH searches for $z > 6$ candidates (Bradley et al. 2013). However, the selection from the deep WFC3/IR imaging yields even fainter candidates, for which the existing ACS imaging is insufficiently deep for confidently excluding lower-redshift interlopers. To alleviate this shortfall, we require that a candidate must not be detected above 1σ in a summed image blueward of the selection bands defined above. For objects at $z \simeq 7$, this requires a non-detection in a summed image of the F606W

¹⁵<http://archive.stsci.edu/hst>

and F435W bands, while for candidates at $z \gtrsim 8$ this requires a non-detection in the stacked optical detection image. We note that forthcoming deeper ACS imaging will allow us to more confidently select faint galaxy candidates, particularly at $z \gtrsim 9$.

In addition to the color selection criteria described above, we also exclude candidates lying within one arcsecond of the detector edges, in order to mitigate potentially spurious photometry. We also exclude candidates lying near stellar diffraction spikes, which are difficult to remove because the individual WFC3/IR exposures were obtained at the same position angle. Finally, we also identify and remove candidates that are brighter than 24 in either IRAC channel, as these are most likely extremely red objects at lower redshift ($z \simeq 2$).

Our *HST* photometry is measured within an isophotal aperture, but aperture-corrected to a total flux using the $mag_{auto} - mag_{iso}$ color in the F160W band. In a few cases where source blending is significant, we visually inspect the images and choose an aperture that is larger than the source's full-width at half-maximum (FWHM), but not so large as to be affected by nearby sources, and use the corresponding aperture magnitude in place of mag_{auto} . We also verify that our aperture colors (and therefore our list of high-redshift candidates) are consistent if we use the publicly released *HST* mosaics based on the *Mosaicdrizzle* pipeline (Koekemoer et al. 2013).¹⁶

In Figure 1 we show image stamps of the six fields containing all nine of our $z > 8$ candidates.

The IRAC images of our candidates suffer from crowding due to the instrument's large point spread function (PSF, FWHM $\simeq 1''.6$), such that simple aperture photometry might result in inaccurate fluxes due to contamination from nearby sources. To address this issue, we use a deblending technique whereby contaminating neighbors are subtracted using *GALFIT* (Peng et al. 2010) by performing a fit to the objects of interest and all their close neighbors simultaneously in a $\sim 10'' \times 10''$ region of fitting window around the source of interest (Overzier et al. 2009; Zheng et al. 2012). The IRAC PSF is determined from the same image by stacking 10 bright, isolated point

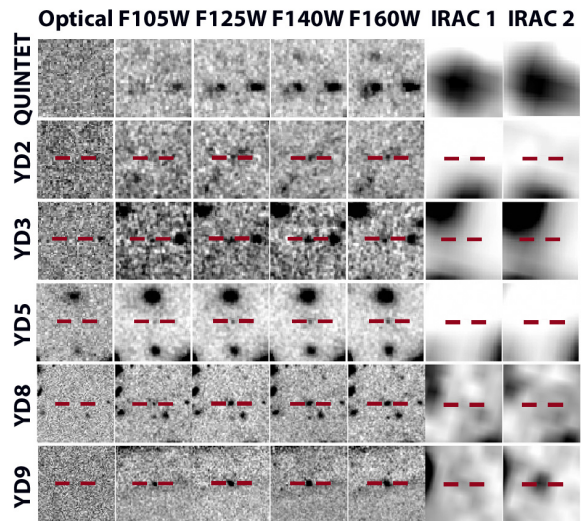


Fig. 1.— Cutout images of LBG candidates of $z \gtrsim 8$ in Abell 2744. The optical images are from the respective ACS detection images, which are the weighted sums of ACS data in the F814W, F606W and F435W bands. For the “Quintet” field, there are multiple candidates including YD1: see Figure 5. For other fields, each candidate is at the image center, marked by a red bar. The field of view is $3''.3$, north is up and east to the left.

¹⁶<http://archive.stsci.edu/pub/hlsp/frontier/abell2744/images/hst/v1.0>

NFW (Navarro, Frenk & White 1996) halo for the dark matter. In the case of A2744, two such elliptical NFW halos are used, centered on the two central, brightest cluster galaxies to represent the global dark-matter component. These are combined with the galaxies component to generate, via a long Monte-Carlo-Markov-Chain minimization, the best-fitting model for the total projected mass (see Zitrin et al. 2013a,b, and references therein).

To estimate the systematic uncertainty in the magnification of each of our high-redshift candidates, we exclude the highest and lowest magnification factors and then calculate the difference in the second-highest and second-lowest magnifications from the different models. This procedure is designed to mitigate potential extremes in the model predictions, and better reflect the true systematic uncertainties. The magnification factors listed in Tables 2, 3, 4 and 6 are the best-fit values at the tabulated redshift based on the ZITRIN “NFW” model, while the uncertainties are the quadrature sum of the systematic and statistical uncertainties. Figure 2 shows the composite color image of the Abell 2744 field, overlaid with the critical curves and identification numbers for all our candidates.

4.2. Photometric Redshifts

We calculate photometric redshifts using the Bayesian photometric redshift code BPZ (Bayesian Photometric Redshifts; Benítez 2000; Coe et al. 2006), adopting the same template library used by the CLASH collaboration (Jouvel et al. 2013). The template set consists of five elliptical galaxy templates, two spiral galaxy templates, and four starburst galaxy templates with moderately strong emission lines. The templates were originally based on the PÉGASE stellar population synthesis models (Fioc & Rocca-Volmerange 1997), but have been recalibrated using spectroscopic redshifts of galaxies with deep, multi-band photometry from the FIREWORKS survey (Wuyts et al. 2008). We assume ignorant (*i.e.*, flat) priors on both galaxy type and redshift in the range $z = 0 - 12$.

Using BPZ, we identify 18 candidates that satisfy our color selection criteria (see §3) and whose photometric redshifts place them at $z > 7$. In Tables 2 and 3 we list the coordinates, photometric redshifts, *HST* photometry, and magnifications of

these 18 candidates. In addition, we identify four more candidates, which also satisfy our color selection criteria but whose photometric redshifts formally place them at $z \simeq 2$ (see Table 4). For these objects, we rerun BPZ assuming that they remain non-detections in the optical bands once the full HFF observations of this cluster field are completed, namely 0.9 magnitude fainter than the current limits (see Table 1). We find that with the deeper optical photometry BPZ places these candidates firmly at $z > 7$. Clearly, the forthcoming deeper optical imaging will be crucial for confirming the high-redshift nature of these latter candidates.

In order to infer the physical properties of our high-redshift candidates (see §5.2), and as an additional check on the BPZ-based photometric redshifts, we use the Bayesian spectral energy distribution (SED) modeling code *iSEDfit* (Moustakas et al. 2013). Using a Monte Carlo technique, we generate 20,000 model SEDs with a broad range of star formation histories, ages, stellar metallicities, dust content, and nebular emission-line strength. We use the Flexible Stellar Population Synthesis models (FSPS, v 2.4; Conroy, Gunn & White 2009; Conroy & Gunn 2010) based on the MILES stellar library (Sanchez-Blázquez et al. 2006) and assume the Chabrier (2003) initial mass function from $0.1 - 100 M_{\odot}$. We adopt *delayed* star formation histories, $\text{SFR}(t) \propto te^{-t/\tau}$, where SFR is the star formation rate, t is the time since the onset of star formation (“age”), and τ is the characteristic time for star formation. The advantage of this parameterization is that it allows for both linearly rising ($t \ll \tau$) and exponentially declining ($t \gtrsim \tau$) star formation histories, which may be important for modeling the SEDs of galaxies at the highest redshifts (e.g., Papovich et al. 2011). For our photometric redshift calculations we adopt uniform priors on age $t \in [0.01, 12]$ Gyr,¹⁸ star formation timescale $\tau \in [0.01, 5.0]$ Gyr, stellar metallicity $Z/Z_{\odot} \in [0.04, 1.6]$, and rest-frame *V*-band attenuation $A_V \in [0 - 3]$ mag, assuming the time-dependent attenuation curve of Charlot & Fall (2000). Each model also includes nebular emission lines whose luminosity is tied self-consistently to the number of hydrogen-ionizing photons.

¹⁸Note that the age of the stellar population is never allowed to be older than the age of the Universe at the redshift under consideration.

We find that `iSEDfit` and BPZ yield statistically consistent photometric redshifts for the majority of the candidates; the mean difference is $\Delta z = 0.08 \pm 0.24$ (`iSEDfit` minus BPZ), which is well within our quoted photometric redshift uncertainties. In a few cases `iSEDfit` prefers a lower-redshift solution, $z \approx 2$; however, in every case these lower-redshift solutions require a highly unlikely combination of physical properties, namely low stellar masses, low star-formation rates, and large amounts of dust attenuation. Secondary peaks in the redshift probability distribution from `iSEDfit`, on the other hand, place these five candidates at $z > 7$, in agreement with BPZ’s primary redshift probability peaks.

4.3. Triple System

To help corroborate the high-redshift nature of our 18 candidates, we search for potential counter images near the locations predicted by the gravitational lensing model. Most of our candidates lie well outside the critical curve, so no counter-images are predicted. The triple system ZD7 is the only case where we convincingly find counter-images at $z > 7$ within our sample, as shown in Figures 2 and 3 and Table 6. Image A is an arclet made of two components that are separated only by ~ 1.5 kpc in the source plane, assuming a magnification of six (see Table 6). This is similar to a case in Abell 1689 where a pair of LBGs at $z \simeq 7.6$ may be merging (Bradley et al. 2008). Image B is behind a bright foreground galaxy, which we subtract before carrying out photometry. We make use of the pure geometric scaling induced by strong lensing to estimate a purely geometric distance for this triply imaged case. The ZITRIN “NFW” lensing model described in §4.1 is based on eleven sets of multiply lensed galaxies between $2 < z < 4$, including a spectroscopic redshift of system 6 at $z = 2.019$ (J. Richard, private communication). This spectroscopic redshift provides a normalization of the model so that the deflection field induced in the lens plane, $\vec{\alpha}_L(\vec{\theta})$, can be scaled to any redshift via the lensing source distance ratio $f(z) = d_{ls}(z)/d_s(z)$ to provide the observed deflection field $\vec{\alpha}(\vec{\theta}) = d_{ls}(z)/d_s(z)\vec{\alpha}_L(\vec{\theta})$. Hence only a simple scaling of the relative lensing distance ratios is required to relate deflections at any given redshift to the lensing distance of the normalization used to calibrate the lens model,

which in our case is $f(z)/f(z = 2.019)$. We find that this factor is ~ 1.12 for the triple system which minimizes the location of the observed images relative to that generated by the model, and this corresponds to a best BPZ estimate of $z \simeq 7.4$. A possible faint fourth image D is noted between images A and B, close to another bright galaxy (Figure 3), although we defer a more detailed analysis of this image once the upcoming deeper ACS observations of Abell 2744 have been completed.

5. DISCUSSION

5.1. Individual Candidates

Our paper serves as an independent verification of dropout objects in other reports, including the recent work of Atek et al. (2013) (A13 hereafter) and Laporte et al. (2014). Most of the 15 candidates in A13 are at $6 < z < 7$, and therefore have only limited overlap with ours. Three of their candidates have been independently identified by us, but with somewhat different photometric redshifts. Object ZD9 in Table 3, with $z_{\text{phot}} = 7.0$, corresponds to A13’s object 561 ($z_{\text{A13}} = 7.5$). Object YD9 ($z_{\text{phot}} = 8.0$) is A13’s object 2070 ($z_{\text{A13}} = 8.35$) and object Y1 ($z = 7.98$) in Laporte et al. (2014). The close pair of ZD3/ZD6 ($z_{\text{phot}} = 7.7$) are marked by A13 as object 2276 ($z_{\text{A13}} = 7.4$).

The IRAC2 flux of object YD9 (Y1 in Laporte et al. 2014) is more than three times the IRAC1 value, which suggests a strong Balmer break. A similar case at $z \simeq 6$ was reported in Abell 383 (Richard et al. 2011) in which both the IRAC1

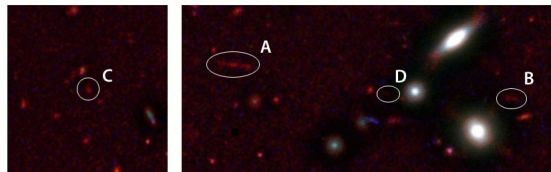


Fig. 3.— Red arclet ZD7 (marked as A) at redshift 7.4 and its two counter images B and C. Both images have been processed to boost the signal-to-noise of faint red objects and to reduce the contribution from nearby bright galaxies. An extremely faint source, marked as D, may be the potential fourth counter image.

and IRAC2 magnitudes are higher than the *HST* photometry by 1.6 magnitude. At redshift $z \simeq 8$, the Balmer break is in the IRAC1 band, and the model prediction is higher than the measured IRAC1 flux.

5.2. Physical Properties

In addition to reporting on the discovery of our high-redshift candidates, we can also begin to characterize their physical properties. We defer a more detailed analysis of the full sample to a forthcoming paper, once the full HFF and ancillary *Spitzer* observations have been completed. Here, we focus on the ten objects at $z > 7$ with the highest-confidence photometric redshifts which have well-measured photometry in at least one IRAC channel. Photometry redward of the Balmer break is particularly important for placing meaningful constraints on the stellar mass and age of the stellar populations in these distant objects.

To infer the physical properties of these galaxies we use *iSEDfit*, but adopt a more restricted set of priors than the ones used to estimate photometric redshifts (see §4.2). Specifically, we adopt uniform priors on galaxy age $t \in [10, 750]$ Myr, $\tau \in [10, 1000]$ Myr, stellar metallicity $Z/Z_{\odot} \in [0.04, 1.0]$, and we assume no dust attenuation (*e.g.*, Bouwens et al. 2010). Recall that the age of the Universe at $z = 7 - 8$ in our adopted concordance cosmology is 750 – 630 Myr.

We find that our $z > 7$ candidates have demagnified stellar masses of around $10^9 M_{\odot}$, and SFRs of approximately $5 M_{\odot} \text{ yr}^{-1}$. These results imply an average doubling time of around 200 Myr, which is roughly one-half the age of the Universe at $z \simeq 8$.¹⁹ The ages of the galaxies in our sample are less well constrained given the uncertainties in our IRAC photometry; nevertheless, we find a median SFR-weighted age for the sample of $\lesssim 350$ Myr (95% confidence interval), corresponding to a typical formation redshift of $z \lesssim 16$. Figure 4 presents the SEDs of four representative galaxies in our sample, sorted by decreasing redshift, as well as the maximum likelihood fits derived using *iSEDfit*.

¹⁹The doubling time is the time it would take to double the stellar mass of the galaxy, where we have assumed that 50% of the stellar mass formed is returned to the interstellar medium via supernovae and stellar winds.

5.3. Source Clustering

An apparent concentration of candidates northeast of the cluster center is shown in Figure 2. Nine objects at $z \simeq 7 - 8$ are found within a region of $20''$. Since the average magnification in that area is not high ($\mu \simeq 1.4$), this apparent overdensity is likely intrinsic rather than being due to lensing. In addition, Figure 5 shows a small region “Quintet” where five candidates are located within approximately $2''$ of one another: objects YD1, YD4, YD6, YD7 and ZD1. These objects have similar estimated photometric redshifts of between 7.9 and 8.6, and their intrinsic separations are within ~ 8 kpc. Given the uncertainties in our photometric redshifts, it is therefore possible that these sources are physically associated.

Overdensities in the high-redshift domain have been previously reported. For example, Trenti et al. (2012) identified four candidates with $z \simeq 8$ within $70''$ in the Field BoRG58. Bradley et al. (2012) found seven LBGs at $z \simeq 7$ in the WFC3/IR field ($\sim 120'' \times 130''$) of Abell 1703. However, our finding of nine LBGs at $7 < z < 9$ within $20''$ (~ 80 kpc in the source plane) is unique, suggesting that the cosmic variance in source density (Trenti & Stiavelli 2008) is more significant than anticipated.

Potentially our most important finding is that the redshift distribution of our sample is not a smoothly declining function towards higher redshift. In particular, our redshift distribution does not extend beyond $z \simeq 9$, clustering notwithstanding, despite the larger window available to $z \simeq 12$ by the deep observed-frame NIR imaging. Interestingly, a similar break at $z \simeq 8$ has been reported for deep-field data, in terms of star formation rate integrated over the limited number of objects that have been uncovered (Bouwens et al. 2011; Oesch et al. 2013). Our break in number density is coincident in redshift but more directly related to formation models than star formation rate. Given the level of clustering that we see here, before a definitive claim can be made regarding a rapid build up in numbers at $z \simeq 8$ it will be important to average over more of the HFF, and to perform a luminosity function analysis so that the redshift dependence can be better related to galaxy mass.

The work presented in this paper is based on observations made with the NASA/ESA *Hubble*

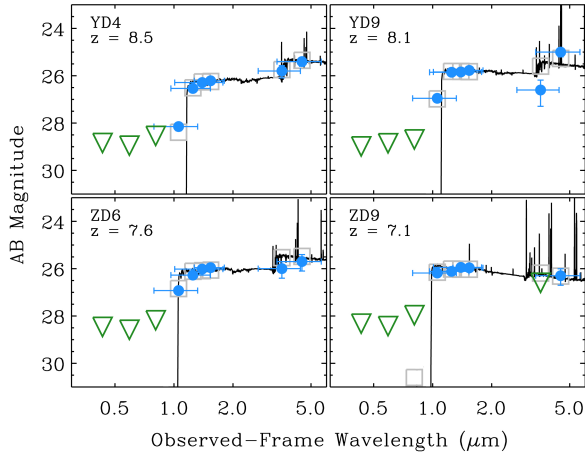


Fig. 4.— Observed-frame SEDs of four bright candidates that have well-measured IRAC photometry. The filled blue points show the observed photometry, while the open green triangles indicate 2σ upper limits. The black spectrum shows the best-fitting (maximum likelihood) SED based on our Bayesian SED modeling using *iSEDfit*. The large gray squares show the photometry of the best-fitting model convolved with the ACS, WFC3, and IRAC filter response curves.

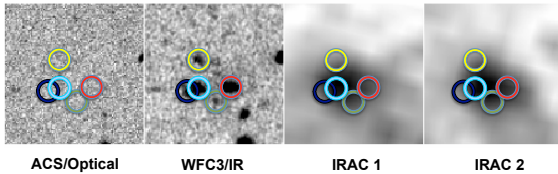


Fig. 5.— “Quintet” of LBGs at $z_{\text{phot}} \approx 8.3$, in an expanded view of the first row in Figure 1. The magnification factor is ~ 1.4 and separations are < 8 kpc in the source plane. The images are of $6''.5$ on each side. The yellow circle marks object YD1; light blue: YD4; dark blue: object YD6; red: object YD7; and green: object ZD1. The circle size is approximately $0''.9$ in diameter. The two *HST* images are the detection images summed over ACS and WFC3/IR bands, respectively. With an IRAC PSF source diameter of $1''.6$ (approximately twice the circles’), these sources are considerably blended. We are able to derive their fluxes or upper limits, assuming fixed source positions in *GALFIT* fitting,

Space Telescope, and has been supported by award AR-13079 from the Space Telescope Science Institute (STScI), which is operated by the Association of Universities for Research in Astronomy, Inc. under NASA contract NAS 5-26555. It is also based on data obtained with the *Spitzer Space Telescope*, which is operated by the Jet Propulsion Laboratory, California Institute of Technology under a contract with NASA. This work utilizes gravitational lensing models produced by P.I.s Bradac, Ebeling, Merten & Zitrin, Sharon, and Williams, funded as part of the *HST* Frontier Fields program conducted by STScI. These models were calibrated using arcs identified in archival *HST* imaging by Merten et al. (2011), spectroscopic redshifts of arcs obtained using the VLT/FORS2 spectrograph (J. Richard et al. 2014, in prep.), and VLT and Subaru/Suprimecam imaging of the Abell 2744 field (Cypriano et al. 2004; Okabe & Umetsu 2008; Okabe, Okura & Futamase 2010; Okabe et al. 2010). XS acknowledges support from FP7-SPACE-2012-ASTRODEEP-312725, and NSFC grants 11103017 and 11233002. Support for AZ is provided by NASA through Hubble Fellowship grant HST-HF-51334.01-A awarded by STScI. FEB acknowledges support from Basal-CATA PFB-06/2007, CONICYT-Chile grants (FONDECYT 1101024, alma-conicyt 31100004, gemini-conicyt 32120003, Anillo ACT1101), and the Millennium Institute of Astrophysics. JMD acknowledges support from the Spanish consoder project CAD2010-00064 and AYA2012-39475-C02-01. We thank R. Smit and M. Meneghetti for helpful comments.

REFERENCES

- Atek, H., Richard, J., Kneib, J.-P. et al. 2013, arXiv 1311.7670 (A13)
- Beckwith, S. V. W., Stiavelli, M., Koekemoer, A. M. et al. 2006, *AJ*, 132, 1729
- Benítez, N., 2000, *ApJ*, 536, 571
- Bertin, E., & Arnouts, S. 1996, *A&AS*, 117, 393
- Blakeslee, J. P., Anderson, K. R., Meurer, G. R., Benítez, N., & Magee, D. 2003, in *Astronomical Data Analysis Software and Systems XII*, ASP Conference Series, Vol. 295, eds. H. E. Payne,

- R. I. Jedrzejewski, & R. N. Hook, (San Francisco: ASP) 257
- Bouwens, R. J., Bradley, L. D., Zitrin, A. et al. 2012*b*, ApJ, submitted, arXiv 1211.2230
- Bouwens, R. J., Illingworth, G. D., Labbe, I. et al. 2011, Nature, 469, 504
- Bouwens, R. J., Illingworth, G. D., Oesch, P. A. et al. 2010, ApJ, 708, L69
- _____ 2012*a*, ApJ, 737, 90
- Bradley, L. D., Bouwens, R. J., Ford, H. C. et al. 2008, ApJ, 678, 647
- Bradley, L. D., Bouwens, R. J., Zitrin, A. et al. 2012, ApJ, 747, 3
- Bradley, L. D., Zitrin, A., Coe, D. et al. 2013, ApJ, submitted, arXiv 1308.1692
- Chabrier, G. 2003, PASP, 115, 763
- Charlot, S. & Fall, S. M. 2000, ApJ, 539, 718
- Coe, D., Benítez, N., Sánchez, S. F., Jee, M., Bouwens, R. & Ford, H. 2006, ApJS, 132, 926
- Coe, D., Zitrin, A., Carrasco, M. et al. 2013, ApJ, 762, 32
- Conray, C. & Gunn, J. E. 2010, ApJ, 712, 833
- Conray, C., Gunn, J. E. & White, M. 2009, ApJ, 699, 486
- Cypriano, E. S., Sodré, L. Jr., Kneib, J.-P. & Campusano, L. E. 2008, ApJ, 613, 95
- Ellis, R. S., McLure, R. J., Dunlop, J. S. et al. 2013, ApJ, 763, L7
- Fazio, G. G., Hora, J. L., Allen, L. E. et al., 2004, ApJS, 154, 10
- Ferguson, H. C. & McGaugh, S. S. 1995, ApJ, 440, 470
- Fioc, M., & Rocca-Volmerange, B. 1997, A&A, 326, 950
- Ford, H. C. & the ACS Science Team 1998, in Space Telescopes and Instruments V, SPIE 3356, eds. P. Y. Bely & J. B. Breckinridge, 234
- Hack, W. J., Dencheva, N., Fruchter, A. S., 2013 in Astronomical Data Analysis Software and Systems XXII, ASP conf. Ser. 475, (San Francisco: ASP) ed. D. Freidel, 49
- Illingworth, G. D., Magee, D., Oesch, P. A. et al. 2013, ApJS, 209, 6
- Laporte, N., Streblyanska, A., Clement, B. et al. 2014, arXiv 1401.8263
- Jouvel, S., Høst, O., Lehav, O., et al. 2013, arXiv:1308.0063
- Kimble, R. A., MacKenty, J. W., O’Connell, R. W., & Townsend, J. A. 2008, in Space Telescopes and Instrumentation 2008: Optical, Infrared, and Millimeter, SPIE 7010, eds. J. M. Oschmann, Jr., M. W. M. de Graauw, & H. A. MacEwen, 70101E
- Koekemoer, A. M., Ellis, R. S., McLure, R. J. et al. 2013, ApJS, 209, 3
- Makovoz, D. & Khan, I. 2005, in Astronomical Data Analysis Software and Systems VI, ASP Conf. Ser. 132, eds. P. L. Shopbell, M. C. Britton, & R. Ebert (San Francisco: ASP), 81
- Merten, J., Coe, D., Dupke, R. et al. 2011, MNRAS, 417, 333
- Moustakas, J., Coil, A., Aird, J. et al. 2013, ApJ, 767, 50
- Navarro, J. F., Frenk, C. S. & White, S. D. M. 1996, ApJ, 462, 563
- Oesch, P. A., Bouwens, R. J., Illingworth, G. D. et al. 2010, ApJ, 709, L16
- _____ 2013, ApJ, 773, 75
- Okabe, N., Okura, Y. & Futamase, T. 2010, ApJ, 713, 291
- Okabe, N., Takada, M., Umetsu, K. et al. 2010, PASJ, 62, 811
- Okabe, N. & Umetsu, K. 2008, PASJ, 60, 345
- Overzier, R. A., Shu, X., Zheng, W. et al. 2009, 704, 548
- Papovich, C., Finkelstein, S. L., Ferguson, H. C., Lotz, J. M., & Giavalisco, M. 2011, MNRAS, 412, 1123

- Peng, C. Y., Ho, L. C., Impey, C. D. & Rix, H.-W. 2010, *AJ*, 139, 2097
- Postman, M., Coe, D., Benítez, N. et al. 2012, *ApJS*, 199, 25
- Redlich, M., Bartemann, M., Waizmann, J.-C. & Fedeli, C. 2012, *A&A*, 547, 66
- Richard, J., Kneib, J.-P., Ebeling, H. et al. 2011, *MNRAS*, 414, L31
- Sanchez-Blázquez, P., Peletier, R. F., Jiménez-Vicente, J. et al. 2006, *MNRAS*, 371, 703
- Torri, E., Meneghetti, M., Bartelmann, M. et al. 2004, *MNRAS*, 349, 476
- Trenti, M., Bradley, L. D., Stiavelli, M. et al. 2012, *ApJ*, 746, 55
- Trenti, M. & Stiavelli, M. 2008, *ApJ*, 676, 767
- Wuyts, S., Labbé, I., Schreiber, N. et al. 2008, *ApJS*, 682, 985
- Zheng, W., Bradley, L. D., Saraff, A. et al. 2012, in *Seventh Conference on Astronomical Data Analysis*, <http://ada7.cosmostat.org/proceedings.php>, 17
- Zheng, W., Postman, M., Zitrin, A. et al. 2012, *Nature*, 489, 406
- Zitrin, A., Broadhurst, T., Umetsu, K. et al. 2009, *MNRAS*, 396, 1895
- Zitrin, A., Menanteau, F., Hughs, J. P. et al. 2013*a*, *ApJ*, 770, L15
- Zitrin, A., Meneghetti, M., Umetsu, K. et al. 2013*b*, *ApJ*, 762, 30

TABLE 1
SUMMARY OF OBSERVATIONS

Telescope	Band	Date	Exposure Time (sec)	Limiting Magnitude (5σ)
<i>HST</i>	F160W	2013 Aug.-Nov.	68202	28.9
<i>HST</i>	F140W	2013 Oct.,Nov.	28140	28.8
<i>HST</i>	F125W	2013 Oct.,Nov.	33048	28.8
<i>HST</i>	F105W	2013 Aug.-Nov.	68952	29.3
<i>HST</i>	F814W	2009 Oct.	13248	28.2
<i>HST</i>	F606W	2009 Oct.	13250	28.7
<i>HST</i>	F435W	2009 Oct.	16162	28.6
<i>Spitzer</i>	IRAC1	2013 Sep.	175104	25.5
		2004 Jun.,Nov.		
<i>Spitzer</i>	IRAC2	2013 Sep.	175104	25.3
		2004 Jun.,Nov.		

TABLE 2
WFC3 AND ACS PHOTOMETRY^a OF CANDIDATES AT $z \gtrsim 8$

Name	Photometric Redshift	RA (J2000)	Dec (J2000)	F160W	F140W	F125W	F105W	F814W	μ^b
YD1	8.6 ± 0.2	3.603856	-30.381905	27.51 ± 0.08	27.46 ± 0.08	27.97 ± 0.14	29.40 ± 0.37	> 30.00	$1.4^{+0.7}_{-0.1}$
YD2	8.5 ± 0.2	3.572515	-30.413267	28.24 ± 0.14	27.91 ± 0.11	28.19 ± 0.15	30.15 ± 0.65	> 30.00	$1.6^{+0.4}_{-0.1}$
YD3 ^d	8.5 ± 0.2	3.591724	-30.380838	28.42 ± 0.15	28.22 ± 0.14	28.68 ± 0.22	30.10 ± 0.59	> 30.00	$1.6^{+1.5}_{-0.1}$
YD4	8.4 ± 0.1	3.603864	-30.382265	26.21 ± 0.03	26.29 ± 0.04	26.54 ± 0.05	28.15 ± 0.17	> 30.00	$1.4^{+0.7}_{-0.1}$
YD5 ^d	$8.3^{+0.2}_{-0.4}$	3.579479	-30.386534	27.77 ± 0.10	27.45 ± 0.09	27.85 ± 0.13	28.94 ± 0.26	29.15 ± 0.69	$3.0^{+9.8}_{-0.9}$
YD6	8.3 ± 0.2	3.604005	-30.382309	26.86 ± 0.05	26.99 ± 0.07	27.13 ± 0.08	28.55 ± 0.21	> 30.00	$1.4^{+0.7}_{-0.1}$
YD7	8.2 ± 0.1	3.603397	-30.382256	25.81 ± 0.03	25.74 ± 0.03	25.99 ± 0.04	27.16 ± 0.08	28.61 ± 0.71	$1.4^{+0.7}_{-0.1}$
YD8	8.1 ± 0.1	3.596096	-30.385832	26.67 ± 0.04	26.55 ± 0.04	26.69 ± 0.04	27.86 ± 0.09	> 30.00	$1.9^{+5.6}_{-0.2}$
YD9 ^{c,d}	8.0 ± 0.1	3.604520	-30.380472	25.77 ± 0.02	25.84 ± 0.03	25.85 ± 0.03	26.95 ± 0.06	> 30.00	$1.3^{+0.7}_{-0.1}$

^aMagnitudes are isophotal, scaled by an aperture correction term derived in the F160W band. The errors and limiting magnitudes are 1σ . Photometric redshifts have been derived using BPZ, and the quoted uncertainties indicate the 68% confidence interval.

^bMagnification factor from ZITRIN “NFW” model (see §4.1), where uncertainties are combined from two sources: (1) the model statistical uncertainties, which are relatively small; and more prominently, (2) the maximum differences with other six models, excluding one highest and one lowest values.

^cReported by A13 and Laporte et al. (2014).

^dGroup 2 as defined in the introduction section, with $z_{\text{phot}} \gtrsim 8$ and a non-negligible probability at low-redshifts.

TABLE 3

WFC3 AND ACS PHOTOMETRY^a OF CANDIDATES AT $7 \lesssim z \lesssim 8$

Name	Photometric Redshift	RA (J2000)	Dec (J2000)	F160W	F140W	F125W	F105W	F814W	μ^b
ZD1 ^d	$7.9^{+0.7}_{-1.7}$	3.603582	-30.382442	29.08 ± 0.24	28.47 ± 0.15	28.94 ± 0.24	30.94 ± 1.08	> 30.00	$1.4^{+0.7}_{-0.1}$
ZD2	7.9 ± 0.2	3.598108	-30.382393	27.77 ± 0.11	27.49 ± 0.09	27.66 ± 0.11	28.49 ± 0.17	> 30.00	$1.5^{+2.3}_{-0.1}$
ZD3 ^c	7.8 ± 0.1	3.606477	-30.380993	26.37 ± 0.04	26.45 ± 0.04	26.45 ± 0.05	27.37 ± 0.08	> 30.00	$1.3^{+1.0}_{-0.1}$
ZD4	7.7 ± 0.5	3.605058	-30.381464	28.15 ± 0.10	28.11 ± 0.11	28.15 ± 0.12	29.18 ± 0.22	29.29 ± 0.54	$1.3^{+0.8}_{-0.1}$
ZD5	$7.7^{+0.1}_{-0.3}$	3.588985	-30.378662	27.39 ± 0.05	27.53 ± 0.06	27.41 ± 0.06	28.15 ± 0.08	> 30.00	$1.6^{+0.9}_{-0.1}$
ZD6 ^c	7.6 ± 0.1	3.606575	-30.380928	25.96 ± 0.04	26.02 ± 0.04	26.27 ± 0.05	26.92 ± 0.07	> 30.00	$1.3^{+1.1}_{-0.1}$
ZD7	$7.4^{+0.1}_{-0.4}$	3.592285	-30.409911	26.98 ± 0.06	26.99 ± 0.07	26.92 ± 0.06	27.39 ± 0.07	> 30.00	$5.9^{+7.8}_{-3.0}$
ZD8 ^d	$7.1^{+0.5}_{-6.2}$	3.576694	-30.383921	28.66 ± 0.15	28.27 ± 0.12	28.55 ± 0.16	29.04 ± 0.18	> 30.00	$2.7^{+3.4}_{-0.6}$
ZD9 ^c	7.0 ± 0.1	3.603208	-30.410368	25.96 ± 0.04	25.94 ± 0.05	26.11 ± 0.05	26.18 ± 0.04	27.97 ± 0.52	$3.4^{+7.8}_{-0.8}$

^aMagnitudes are isophotal, scaled by an aperture correction term derived in the F160W band. The errors and limiting magnitudes are 1σ . Photometric redshifts are BPZ with 1σ error.

^bMagnification factor from ZITRIN “NFW” model (see §4.1), where uncertainties are combined from two sources: (1) the model statistical uncertainties, which are relatively small; and more prominently, (2) the maximum differences with other six models, excluding one highest and one lowest values.

^cReported by A13.

^dGroup 2 as defined in the introduction section, with $z_{\text{phot}} \gtrsim 8$ and a non-negligible probability at low-redshifts.

TABLE 4
WFC3 AND ACS PHOTOMETRY^a OF POSSIBLE CANDIDATES

Name	RA (J2000)	Dec (J2000)	F160W	F140W	F125W	F105W	F814W	μ^b
PD1	3.572891	-30.413647	27.70 ± 0.13	27.50 ± 0.12	28.02 ± 0.20	28.64 ± 0.25	> 30.00	$1.6^{+0.5}_{-0.1}$
PD2	3.605268	-30.380613	27.88 ± 0.13	27.92 ± 0.14	28.22 ± 0.18	29.08 ± 0.31	> 30.00	$1.3^{+0.7}_{-0.1}$
PD3	3.576291	-30.409891	27.59 ± 0.07	27.75 ± 0.09	27.85 ± 0.10	28.36 ± 0.12	> 30.00	$2.3^{+2.1}_{-0.3}$
PD4	3.567849	-30.411451	27.90 ± 0.12	27.79 ± 0.11	28.42 ± 0.21	28.28 ± 0.14	29.36 ± 1.15	$1.5^{+0.5}_{-0.1}$

^aMagnitudes are isophotal, scaled by an aperture correction term derived in the F160W band. The errors and limiting magnitudes are 1σ . These objects have their estimated photometric redshifts less than 7 based on the existing data, but meet our selection criteria. They are subject to further examinations.

^bMagnification factor from ZITRIN “NFW” model (see §4.1), where uncertainties are combined from two sources: (1) the model statistical uncertainties, which are relatively small; and more prominently, (2) the maximum differences with other six models, excluding one highest and one lowest values.

TABLE 5
IRAC PHOTOMETRY FOR SELECTED CANDIDATES

Name	IRAC 1	IRAC 2
YD1	> 27.3	26.2 ± 0.5
YD2	> 27.3	> 27.1
YD4 ^a	25.8 ± 0.3	25.4 ± 0.2
YD6	25.5 ± 0.2	25.2 ± 0.2
YD6 ^a	26.5 ± 0.6	26.2 ± 0.5
YD8	> 27.3	> 27.1
YD9	26.6 ± 0.7	25.0 ± 0.2
ZD1	25.7 ± 0.3	26.1 ± 0.5
ZD2	> 27.3	> 27.1
ZD3 ^a	26.5 ± 0.6	26.1 ± 0.5
ZD4	26.1 ± 0.4	25.9 ± 0.4
ZD6 ^a	26.0 ± 0.4	25.7 ± 0.4
ZD8	> 27.3	> 27.1
ZD9	> 27.3	26.3 ± 0.4
PD1	> 27.3	> 27.1
PD2	> 27.3	> 27.1
PD3	> 27.3	> 27.1
PD4	26.2 ± 0.6	> 27.1

^aTwo respective close pairs within one IRAC pixel, each fitted as one component. The fluxes of individual components are partitioned by a ratio of their fluxes in the F160W band.

TABLE 6
PHOTOMETRY^a OF TRIPLE SYSTEM

Name	RA (J2000)	Dec (J2000)	F125W	F160W-F125W	F140W-F125W	F105W-F125W	F814W-F125W	μ^b
ZD7A1	3.592410	-30.409897	27.30 ± 0.07	0.06 ± 0.10	0.06 ± 0.10	0.41 ± 0.11	> 2.64	5.7 ^{+7.5} _{-2.7}
ZD7A2	3.592160	-30.409925	28.26 ± 0.11	0.04 ± 0.15	0.06 ± 0.15	0.74 ± 0.16	> 2.74	6.4 ^{+13.2} _{-3.4}
ZD7B	3.588430	-30.410340	27.6 ± 0.1	0.1 ± 0.1	0.1 ± 0.1	0.8 ± 0.3	> 1.1	32.5 ⁺³¹ ₋₃₂
ZD7C	3.600940	-30.400824	29.15 ± 0.18	0.08 ± 0.25	-0.25 ± 0.23	0.72 ± 0.31	> 0.86	2.8 ^{+1.5} _{-0.1}

^aMagnitudes are isophotal, scaled by an aperture correction term derived in the F160W band. The errors and limiting magnitudes are 1σ .

^bMagnification factor from ZITRIN “NFW” model (see §4.1), where uncertainties are combined from two sources: (1) the model statistical uncertainties, which are relatively small; and more prominently, (2) the maximum differences with other six models, excluding one highest and one lowest values.